Coherent optical and spin spectroscopy of nanoscale Pr^{3+} : Y_2O_3

D. Serrano,[1] C. Deshmukh,[2] S. Liu,[1] A. Tallaire,[1] A. Ferrier,[1,3] H. de Riedmatten,[2,4] and P. Goldner[1]

[1]*Chimie ParisTech, PSL University, CNRS, Institut de Recherche de Chimie Paris, F-75005 Paris, France*

[2]*Institut de Ciencies Fotoniques, The Barcelona Institute of Science and Technology, 08860 Castelldefels, Barcelona, Spain*

[3]*Sorbonne Université, Faculté des Sciences et Ingénierie, UFR 933, F-75005 Paris, France*

[4]*Institució Catalana de Recerca i Estudis Avançats, 08015 Barcelona, Spain*

(Received 31 July 2019; revised manuscript received 19 September 2019; published 4 October 2019)

We investigate the potential for optical quantum technologies of Pr^{3+} : Y_2O_3 in the form of monodisperse spherical nanoparticles. We measured optical inhomogeneous lines of 27 GHz and optical homogeneous linewidths of 108 and 315 kHz in particles with 400- and 150-nm average diameters, respectively, for the $^1D_2(0) \leftrightarrow {}^3H_4(0)$ transition at 1.4 K. Furthermore, ground-state and $^1D_2$ excited-state hyperfine structures in Y_2O_3 are here determined by spectral hole burning and modeled by complete Hamiltonian calculations. Ground-state spin transitions have energies of 5.99 and 10.42 MHz, for which we demonstrate spin inhomogeneous linewidths of 42 and 45 kHz, respectively. Spin T_2 up to 880 μs was obtained for the $\pm 3/2 \leftrightarrow \pm 5/2$ transition at 10.42 MHz, a value which exceeds that of bulk Pr^{3+}-doped crystals reported so far. These promising results confirm nanoscale Pr^{3+} : Y_2O_3 is a very appealing candidate to integrate quantum devices. In particular, we discuss the possibility of using this material for realizing spin-photon interfaces emitting indistinguishable single photons.

DOI: 10.1103/PhysRevB.100.144304

I. INTRODUCTION

Solid-state spins are extensively investigated for quantum-state storage, quantum computation, and quantum communications [1–4]. Among them, rare-earth (RE) spins stand out for presenting electron and/or nuclear spin states with outstandingly long coherence lifetimes T_2 at cryogenic temperatures [5–7]. Moreover, RE spins are optically accessible through coherent optical transitions [8], a unique feature in the solid state which makes them optimum candidates for quantum spin-photon interfaces [9]. In recent years, the potential of RE materials for quantum technologies has been supported by achievements such as high-efficiency optical quantum memories [10], quantum teleportation [11], multimode spin-wave storage [12], and high-fidelity quantum-state tomography [13]. However, an important challenge in bulk crystals remains addressing single RE ions, a key point for the development of scalable quantum architectures [14–16]. This is due, on the one hand, to the long population lifetimes of $4f$-$4f$ optical transitions and, on the other hand, to the difficulty isolating a single RE ion within a macroscopic crystal [17,18]. A promising approach to overcome these difficulties consists of coupling RE emitters in nanocrystals to high-quality-factor optical microcavities [19]. In particular, using nanoscale crystals facilitates reaching the single-emitter level [18], whereas the cavity coupling provides stronger light-matter interactions [15,20] and Purcell-enhanced spontaneous emission rates [19].

Exploiting this approach to build novel quantum devices strongly relies on developing RE nanocrystals with narrow optical and spin homogeneous lines. Those are not straightforwardly available as nanomaterials and often show additional homogeneous linewidth broadening, i.e., T_2 shortening, due to surface states and modified spin bath dynamics [21–23]. Still, very promising results were recently obtained with chemically synthesized $^{151}Eu^{3+}$-doped Y_2O_3 nanocrystals. Y_2O_3 is a low-magnetic-moment density host which can be obtained with accurate control over particle size and morphology [24,25]. More important, optical homogeneous linewidths down to 25 kHz have been reported in these nanocrystals for the $^7F_0 \leftrightarrow {}^5D_0$ transition at 580.883 nm [25,26] and millisecond-long nuclear spin T_2 [27]. A disadvantage of Eu^{3+} is, however, that it presents weak oscillator strength ($\sim 10^{-8}$ in Y_2O_3 [28]) and a low emission branching ratio for the $^7F_0 \leftrightarrow {}^5D_0$ line ($\sim$0.016 [19]). This reduces the achievable Purcell enhancement by a factor of 60 for this ion [19]. In these aspects, a good alternative rare-earth ion to Eu^{3+} is Pr^{3+}. In Y_2O_3, the Pr^{3+} : $^1D_2(0) \leftrightarrow {}^3H_4(0)$ transition is expected to exhibit an oscillator strength at least one order of magnitude larger than the Eu^{3+} : $^7F_0 \leftrightarrow {}^5D_0$ transition [28,29]. A higher emission branching ratio is equally expected from luminescence investigations carried out on this compound [30]. However, very few previous studies exist on optical homogeneous lines in Pr^{3+} : Y_2O_3 [31–33], and hyperfine structures and spin homogeneous lines have not been reported.

In the present work, we carry out a complete high-resolution and coherent optical and nuclear spin spectroscopic investigation of $^{141}Pr^{3+}$: Y_2O_3 ceramics and nanoparticles. This paper is organized as follows: experimental details and methods are given in Sec. II. In Sec. III A, optical inhomogeneous and homogeneous linewidths results are shown and discussed. We next present the experimental investigation of the $^{141}Pr^{3+}$ hyperfine structures in Y_2O_3 (Sec. III B). That is followed by hyperfine-structure and g factor calculations

in Sec. III C. In Sec. III D, spin resonance results are reported, from which we derive ground-state spin inhomogeneous linewidths and coherence lifetimes. Finally, a summary of the results and a discussion of the potential of $Pr^{3+}:Y_2O_3$ for quantum technologies applications are given in Sec. III E.

II. EXPERIMENT

Two batches of monodispersed spherical 0.05% $Pr^{3+}:Y_2O_3$ nanoparticles were synthesized by homogeneous precipitation with average particle sizes of 400 and 150 nm and crystalline domains of 120 and 80 nm, respectively, as determined by x-ray diffraction [24]. Postsynthesis, the particles were placed onto a glass plate and submitted twice to a pure oxygen plasma for 3 min. A homemade system operating at a frequency of 2.45 GHz, a microwave power of 900 W, and a pressure of 1 mbar was used [25,34]. In addition, a $Pr^{3+}:Y_2O_3$ bulk ceramic sample (0.05 at. %) with micrometer-size crystalline domains was elaborated by mixing stoichiometric Y_2O_3 and Pr_6O_{11} oxides (99.99% purity) and by pressing these powders into pellets, followed by sintering at 1500 °C for 48 h. Particles and ceramics were obtained with a pure cubic phase (Ia-3 space group), where Pr^{3+} ions replace Y^{3+} cations at the C_{3i} and C_2 point symmetry sites [33]. In the following, we will focus on the spectroscopic properties of Pr^{3+} ions occupying C_2 sites.

Low-temperature, high-resolution, and coherent spectroscopy investigations were carried out on ensembles of nanoparticles in the form of loose powders. Those were placed in a custom-made container about 500 μm thick, presenting front and rear optical access. The bulk ceramic sample was cut into 250-μm slices and attached to a flat sample holder with a transmission opening for measurements. Nanoparticles and ceramic samples, in their respective containers or holders, were introduced into a He bath cryostat (Janis SVT-200) operated in liquid mode for $T < 2$ K and gas flow mode for $T > 2$ K. The temperature was monitored directly on the sample holders by a Si diode (Lakeshore DT-670). Excitation was provided by a cw dye laser (Sirah Matisse DS) with an ~200-kHz linewidth. Pulsed sequences required for spectral hole burning and spin-echo and photon-echo measurements (Fig. 1) were created by modulating the cw laser output with two acousto-optic modulators driven by an arbitrary wave form generator (Agilent N8242A). For more details, refer to the optical setup scheme and description in Ref. [27]. Light emerging from the backside of the samples was collected by a series of lenses, as proposed in [35] for highly scattering media, and focused on an avalanche photodiode (Thorlabs A/M110) for detection.

Photoluminescence (PL) and absorption measurements were performed with an optical closed-cycle cryostat. PL spectra were recorded at 10 K under 460-nm excitation ($^3H_4 \rightarrow {}^3P_1, {}^1I_6$) by an optical parametric oscillator pumped by the third harmonic (355 nm) of a Nd:YAG laser (Ekspla NT342B). Emitted light was sent to a spectrometer (Acton SP2300) and detected by a cooled-down CCD camera (Princeton Instruments). The $Pr^{3+}:Y_2O_3$ absorption spectrum was acquired at 15 K from a 28-mm-thick transparent ceramic, using a Varian Cary 6000i spectrophotometer. The integrated absorption coefficient for the $^3H_4(0) \rightarrow {}^1D_2(0)$ transition enabled calculating the transition oscillator strength, from which we determined the transition branching ratio (see Sec. III E).

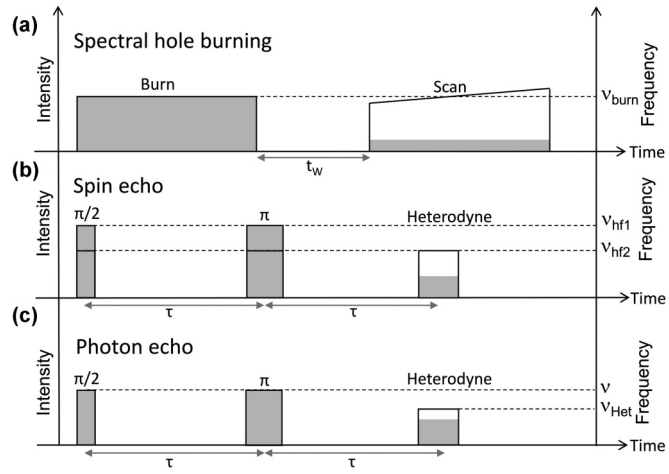

FIG. 1. Pulse sequences. (a) Spectral hole burning sequence. (b) Two-pulse Raman spin-echo sequence. The spin-echo amplitude at 2τ is probed by a single-frequency pulse referred to as a heterodyne pulse. (c) Two-pulse photon-echo sequence with heterodyne detection. We note that the role of the heterodyne pulse is not the same in (b) and (c). In (c), it is used as a local oscillator, while in (b) it also converts spin coherence into an optical one for detection. Thus, in the latter case, its frequency must match one of the two colors in the bifrequency pulses (either ν_{hf1} or ν_{hf2}). Typical pulse lengths are hundreds of microseconds in (a), tens of microseconds in (b), and hundreds of nanoseconds in (c). Gray areas represent pulse intensities, and black lines show pulse frequencies.

Optical inhomogeneous lines Γ_{inh} were measured at 12 K for the $^3H_4(0) \rightarrow {}^1D_2(0)$ optical transition, where 0 refers to the lowest energy levels in the $^3H_4$ and $^1D_2$ electronic multiplets. The line profile was obtained by photoluminescence excitation by collecting $^1D_2$ emissions while scanning the cw laser wavelength around the peak maximum at $\lambda_{vac} = 619.011$ nm. A long-pass filter was placed in front of the detector to filter out excitation light. Persistent spectral holes were burned at 1.4 K by a single 500-μs-long pulse and then probed at time t_W by monitoring the transmission intensity of a weak scanning pulse [Fig. 1(a)]. The waiting time t_W is set so that $t_W > \tau_{1D2}$, with τ_{1D2} being the $^1D_2$ excited-state population lifetime or optical T_1. Spin inhomogeneous and homogeneous lines were obtained at 1.4 K from two-pulse Raman spin echoes [Fig. 1(b)]. A spin population difference was first induced by optically pumping a subensemble of ions from one spin level to the other one [27]. Then, two-color laser pulses were applied to create and rephase spin coherences. The spin inhomogeneous line was measured by varying the frequency detuning between the two colors ($\nu_{hf1} - \nu_{hf2}$) while keeping a fixed pulse delay τ [27]. Spin T_2 values were directly derived from the decay of the spin-echo amplitude when increasing τ. Finally, optical coherence lifetimes were measured for the $^3H_4(0) \leftrightarrow {}^1D_2(0)$ transition at 1.4 K by two-pulse photon-echo spectroscopy with heterodyne detection [35] [Fig. 1(c)]. The π-pulse lengths were set to 15 μs in

Fig. 1(b) and 700 ns in Fig. 1(c), with an input power of approximately 50 mW.

III. RESULTS

A. Optical inhomogeneous and homogeneous linewidths

The $^3H_4(0) \leftrightarrow {}^1D_2(0)$ optical inhomogeneous lines are displayed in Fig. 2(a) for the ceramic and 400-nm-diameter nanoparticles. The ceramic sample shows a FWHM of 9 GHz and has a Lorentzian profile. This is consistent with previous investigations on bulk Y_2O_3 : Pr^{3+} [33] and Y_2SiO_5 : Pr^{3+} [36]. In opposition, a line three times broader, i.e., 27 GHz, was obtained in the nanoparticles case. This line broadening is due to the postsynthesis O_2 plasma treatment. Indeed, similar behavior is observed in Eu^{3+} : Y_2O_3 nanoparticles: bulk-like inhomogeneous lines are measured after synthesis [26], whereas a factor of 2–3 line broadening is observed following O_2 plasma processing [25]. The processing also provokes a blueshift of about 10 GHz from 484.308 THz ($\lambda_{vac} =$ 619.011 nm), as measured in the ceramic, to 484.317 THz.

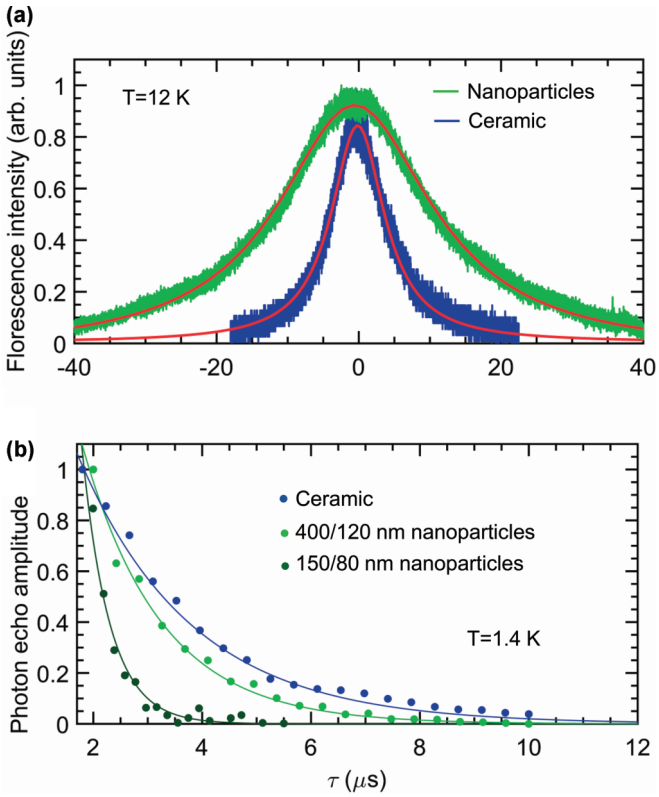

FIG. 2. Optical inhomogeneous lines and coherence lifetimes. (a) Optical inhomogeneous lines for the $^3H_4(0) \leftrightarrow {}^1D_2(0)$ transition for ceramic (blue line) and 400-/120-nm-diameter particles/crystallites (green line). Red lines correspond to Lorentzian fits. Zero-frequency detuning stands for 484.308 THz for the ceramic and 484.317 THz for nanoparticles. (b) Photon echo decays from ceramic (blue), 400-/120-nm-diameter particles/crystallites (green) and 150-/80-nm-diameter particles/crystallites (dark green). All decays show single-exponential character; therefore, optical T_2 values of 4.5 ± 0.5, 3.0 ± 0.3, and 1.0 ± 0.1 μs were obtained by fitting the photon-echo amplitudes to $\exp(-2\tau/T_2)$ (lines). The resulting homogeneous lines correspond to 72 ± 16, 108 ± 21, and 315 ± 64 kHz for ceramic, 400-nm, and 150-nm particles, respectively.

Shift and broadening are attributed to strain induced by the increased oxygen content in the nanoparticles under O_2 plasma treatment [34].

While the plasma processing broadens the optical inhomogeneous line, it has a positive impact on the Pr^{3+} optical coherence lifetime. Indeed, longer coherence lifetimes are found after O_2 plasma processing. In particular, coherence lifetimes of 3 and 1 μs [Fig. 2(b)], corresponding to homogeneous lines $\Gamma_h = (\pi T_2)^{-1}$ of 108 and 315 kHz, were obtained in 400- and 150-nm-diameter particles, respectively. This is about a factor of 2 less than homogeneous linewidths obtained immediately after synthesis. Moreover, these values are narrower than those reported in some particular bulk Pr^{3+} : Y_2O_3 crystals [33], although they still remain far from the 1.1-kHz linewidth given by the optical T_1 limit. T_1 is found to be equal to 140 μs in the nanoparticles, which is similar to bulk Pr^{3+} : Y_2O_3 [30]. The decay curve is shown in Sec. III E.

In a previous work, the dominant optical dephasing mechanism in Eu^{3+} : Y_2O_3 nanoparticles was attributed to fluctuating electric fields associated with charged surface states [26]. The broader homogeneous line found here for the 150-nm-diameter particles [Fig. 2(b)] is consistent with this hypothesis since surface-to-volume ratios increase as the particle size decreases [26]. Nonetheless, it seems that the observed broadening is better explained by the decrease in crystalline grain size rather than particle size. Crystalline domains decrease from 120 to 80 nm for 400- to 150-nm-diameter particles. Therefore, the electric field strength ($\mathbf{E} \propto r^{-2}$) at the center of a crystallite is about 2.3 times larger in an 80-nm crystallite than in a 120-nm one. This assumes that the field originates from electric charges located at the interface between crystallites. In contrast, if we take into account electric noise originating at the nanoparticle outer surface, an electric field strength that is seven times larger is expected in the 150-nm particles. This should lead to larger broadening than experimentally observed. In a similar way, the impact of the crystalline domain size over the particle size in optical dephasing was recently evidenced in $Eu^{3+}Y_2O_3$ nanoparticles [25].

B. Spectral hole burning

With a single nuclear isotope and nuclear spin $I = 5/2$, the $^{141}Pr^{3+}$ hyperfine structure at zero magnetic field consists of three doubly degenerate levels, namely, $\pm 1/2$, $\pm 3/2$, and $\pm 5/2$ [36]. The hyperfine energy splittings in Y_2O_3 were obtained for the $^3H_4(0)$ ground-state and $^1D_2(0)$ excited-state energy levels by spectral hole burning (SHB). The recorded SHB spectrum is displayed in Fig. 3(a), with the main hole appearing at the center surrounded by side holes and antiholes. We derived the excited-state splittings from the side hole position [37], finding that it corresponds to 2.9 and 1.4 MHz. The antiholes at 6, 10.4, and 16.4 MHz reveal the ground-state $\pm 1/2 \leftrightarrow \pm 3/2$, $\pm 3/2 \leftrightarrow \pm 5/2$, and $\pm 1/2 \leftrightarrow \pm 5/2$ hyperfine splittings, respectively. A simulated spectrum computed with the mentioned ground- and excited-state hyperfine splittings shows very good agreement with the experiment. More accurate values for the ground-state hyperfine splittings, up to 10-kHz precision, are given in Sec. III D, derived from spin resonance investigations. Ground- and excited-state energy schemes are shown in Fig. 4.

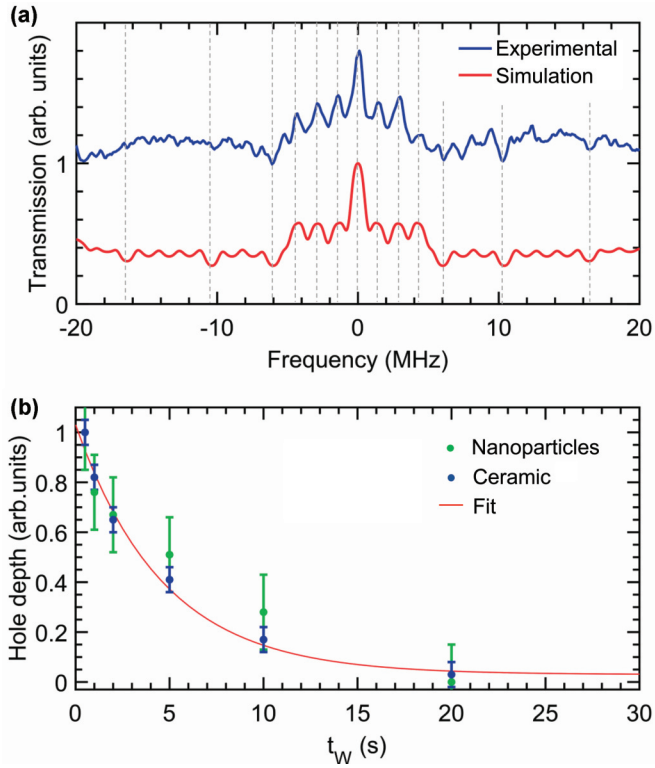

FIG. 3. Hyperfine level structure and spin population lifetime. (a) Single-shot spectral hole burning spectrum from Pr^{3+} : Y_2O_3 ceramic (blue) compared to simulation (red). Main transitions are indicated by dashed lines. (b) Hole decay as a function of waiting time before readout t_W as measured for ceramic (green dots) and 400-/120-nm particles (blue dots). Single-exponential fit to the ceramic data reveals a spin relaxation time of 5 ± 1 s (red line).

The central hole decay as a function of time is shown in Fig. 3(b). The hole lifetime is estimated to 5 ± 1 s by a single-exponential fit to the ceramic data. A single-exponential fit results in a longer decay time for the nanoparticles (7 ± 3 s). Nevertheless, the difference is not considered significant as it falls within experimental error bars. Those are quite important, especially in the nanoparticle case, due to the strong light scattering at the samples resulting in rather low signal-to-noise ratios. The measured hole decay time results from a combination of different population decay rates among the three ground-state hyperfine levels [38]. Still, it provides a good indication of the spin relaxation time T_1. The obtained values are comparable to those reported for other Pr^{3+} doped crystals such as $YAlO_3$ and $La_2(WO_4)_3$ [38,39]. They are, however, two orders of magnitude lower than values typically reported for Pr^{3+} : Y_2SiO_5 [40], although a shorter T_1 component of 7 s has also been observed in this crystal [41,42].

C. Hyperfine structures and *g* factor calculation

The energy level structure of rare-earth ions is the result of several interactions which can be listed as

$$H = [H_{FI} + H_{CF}] + [H_{HF} + H_Q + H_Z + H_z]. \quad (1)$$

The first bracketed term, including the free-ion Hamiltonian H_{FI} and the crystal-field Hamiltonian H_{CF}, determines the

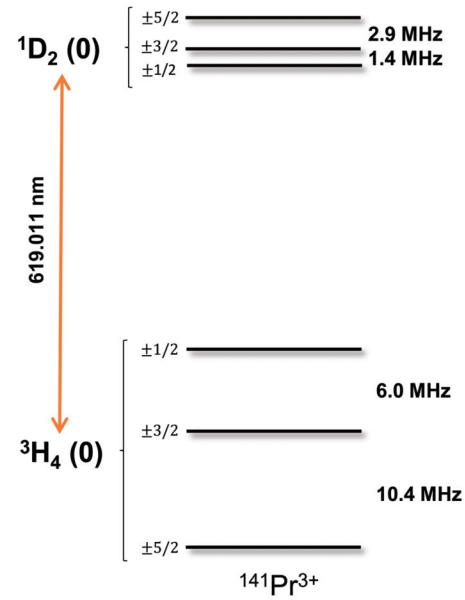

FIG. 4. Measured hyperfine structure in ^{141}Pr : Y_2O_3 ($I = 5/2$). The $\pm M_I$ quantum numbers are used only as labels and do not represent actual eigenstate projections.

energies and wave functions of the so-called crystal field levels. The second term is formed by the hyperfine interaction H_{HF}, the nuclear quadrupole interaction H_Q, and the electron (H_Z) and nuclear (H_z) Zeeman interactions. For non-Kramers RE ions, i.e., with an even number of f electrons, electron Zeeman and hyperfine interactions have zero diagonal matrix elements for nondegenerate crystal-field (CF) levels. This is the case for Pr^{3+} ions in C_2 site symmetry. When such levels are separated from other CF levels by more than a few cm^{-1}, electron Zeeman and hyperfine interactions have only second-order contributions to hyperfine structures, resulting in splittings on the order of tens to hundreds of MHz [37].

Previous work showed that experimental rare-earth fine and hyperfine structures can be well reproduced by the Hamiltonian in Eq. (1). Some examples are Pr^{3+}-doped [39,43], Er^{3+}-doped, [44,45], and Ho^{3+}-doped [46] crystals. Following our work on Pr^{3+}-doped $LiYF_4$ [37] and $La_2(WO_4)_3$ [43], hyperfine structures in Y_2O_3 were computed by directly diagonalizing the Hamiltonian in Eq. (1). For H_{FI} and H_{CF}, we used the parameters determined by Morrison *et al.* in an extensive study of CF energy levels modeled in RE-doped Y_2O_3 [28]. Matrix elements of $H_{HF} + H_Q + H_Z + H_z$ were then evaluated using the following equations [43,47]:

$$H_{HF} = a_1 H_1, \quad (2)$$

$$H_Q = a_2 H_2 + a_3 H_3, \quad (3)$$

$$H_Z = \mu_B \mathbf{B} \cdot (\mathbf{L} + g_e \mathbf{S}), \quad (4)$$

$$H_z = -g_n \mu_n \mathbf{B} \cdot \mathbf{I}, \quad (5)$$

where μ_b and μ_n are the Bohr and nuclear magnetons; **B** is an external magnetic field; **L**, **S**, and **I**, are the orbital,

TABLE I. Experimental and calculated hyperfine splittings at zero magnetic field for ground $^3H_4(1)$ and excited $^1D_2(1)$ states of $^{141}Pr^{3+}$ in Y_2O_3 (C_2 site), $La_2(WO_4)_3$ [39], and Y_2SiO_5 (site 1) [36].

	Y_2O_3		$La_2(WO_4)_3$	Y_2SiO_5
	Expt. (MHz)	Calculation (MHz)	Expt. (MHz)	Expt. (MHz)
$^3H_4$	6.0	5.4	14.90	10.19
	10.4	10.7	24.44	17.30
$^1D_2$	1.4	1.5	4.94	4.59
	2.9	2.9	7.23	4.84

TABLE II. Ground- and excited-state spin Hamiltonian parameters fitted to calculated hyperfine splittings under a magnetic field of 5 mT whose directions follow the surface of a sphere.

Parameter	Ground state	Excited state
D (MHz)	−2.66	0.72
$\|E\|$ (MHz)	0.2	0.078
$\|g_1\|$ (MHz/T)	13.9	10.8
$\|g_2\|$ (MHz/T)	18.6	12.9
$\|g_3\|$ (MHz/T)	84.7	14.9

electron, and nuclear spin angular momenta; g_e is the electron g factor; and $g_n = 1.6$ is the nuclear g factor of $^{141}Pr^{3+}$. Matrix elements of H_1 are given in [48]. Matrix elements for H_2 and H_3 can be found in Ref. [43]. The definitions of a_i are given in the Appendix. These a_i, which contain several parameters not precisely known like $4f$-electron radius and screening factors, were adjusted to give the best fit to the $^3H_4(0)$ and $^1D_2(0)$ experimental hyperfine splittings (Fig. 4). The resulting values are $a_1 = 660$ MHz, $a_2 = 18.6$ MHz, and $a_3 = 4.7 \times 10^{-8}$. Note that a_3, which corresponds to the lattice contribution to the quadrupole interaction, is dimensionless, whereas rank-2 CF parameters appear in H_3. These values are reasonably close to those determined in previous studies. For example, in Pr^{3+} : $La_2(WO_4)_3$, $a_1 = 721$ MHz, $a_2 = 26.9$ MHz, and $a_3 = 1.7 \times 10^{-7}$ [43].

We first discuss the zero-field case, i.e., $\mathbf{B} = 0$ in Eqs. (4) and (5). The calculated and experimental splittings, in good agreement, are shown in Table I. In opposition to Pr^{3+} : $La_2(WO_4)_3$, the excited-state splittings were correctly calculated using the $^1D_2(0)$ CF level and not $^1D_2(1)$. This suggests a more accurate CF analysis in the case of Pr^{3+} : Y_2O_3 in which the true site symmetry C_2 was used, whereas a C_{2v} symmetry was substituted for C_1 in Pr^{3+} : $La_2(WO_4)_3$ [43]. Diagonalizing the total Hamiltonian of Eq. (1) when setting the quadrupolar interaction H_Q to zero shows that ground-state splittings are dominated by the hyperfine interaction, which gives more than 90% of the observed values. In the excited state, however, it has a contribution lower than 0.2 MHz. This is consistent with the hyperfine interaction being a second-order perturbation: the ground-state first CF level energies (0, 108, 291, 345 cm^{-1}) are closer than the excited ones (0, 267, 711 cm^{-1}), which qualitatively explains the difference in the hyperfine contribution. A more precise assessment would take into account matrix elements of the form $\langle n|J_i|n'\rangle\langle n'|J_j|n\rangle$, where n, n' denote CF levels of the multiplet of interest and $J_{i,j}$, with $i, j = x, y, z$, is the total angular momentum along the CF axes [39]. The low hyperfine contribution shows that the excited-state splittings are mainly due to the quadrupole interaction. This one has two parts that correspond to the interaction between the nuclear quadrupole moment and the electric field gradient created, on the one hand, by the f electrons and, on the other hand, by the lattice electrons [a_2H_2 and a_3H_3 in Eq. (3), respectively]. Setting them to zero alternatively suggests that they have contributions of opposite signs. This gives small excited-state splittings in comparison with Pr^{3+} in $La_2(WO_4)_3$ and in site 1 of Y_2SiO_5 (Table I). The same holds for the ground-state splittings, which is likely to be explained by the larger CF splittings for Pr^{3+} in Y_2O_3 (0, 108, 291, 345 cm^{-1}) than in $La_2(WO_4)_3$ (0, 59, 91,168 cm^{-1}) [43] or Y_2SiO_5 (0, 88, 146 cm^{-1}) [36].

Applying an external magnetic field removes the twofold degeneracy of each hyperfine level because of the hyperfine and electron Zeeman second-order cross term and the nuclear Zeeman one. To determine the $^{141}Pr^{3+}$ corresponding gyromagnetic factors, we switched to a spin Hamiltonian approach, in which the hyperfine structure of a given CF level is given by the Hamiltonian

$$H_s = \mathbf{B}\cdot\mathbf{M}\cdot\mathbf{I} + \mathbf{I}\cdot\mathbf{Q}\cdot\mathbf{I}, \tag{6}$$

where $\mathbf{M}$ and $\mathbf{Q}$ are the effective Zeeman and quadrupolar tensors. In their respective principal axes, the $\mathbf{M}$ and $\mathbf{Q}$ tensors read

$$\mathbf{M} = \begin{pmatrix} g_1 & 0 & 0 \\ 0 & g_2 & 0 \\ 0 & & g_3 \end{pmatrix}, \tag{7}$$

$$\mathbf{Q} = \begin{pmatrix} E - \frac{1}{3}D & 0 & 0 \\ 0 & -E - \frac{1}{3}D & 0 \\ 0 & & \frac{2}{3}D \end{pmatrix}. \tag{8}$$

One principal axis of both tensors coincides with the site C_2 symmetry axis. The g_i, D, and E values were determined by a fit to the calculated hyperfine splittings given by the Hamiltonian in Eq. (1) with a fixed magnetic field magnitude of 5 mT and a direction that spanned a sphere in the CF axis system, as in previous experiments [39,49]. The fitted parameters are given in Table II. The largest ground-state gyromagnetic factor is 85 MHz/T and results mainly from the second-order perturbation as the nuclear Zeeman contribution is only 12.2 MHz/T. It is smaller than the values for $La_2(WO_4)_3$ (147 MHz/T) [39] and Y_2SiO_5 (113 MHz/T) [49,50]. This can again be explained by the larger CF splittings in Y_2O_3 that reduce second-order effects. In the excited state, the gyromagnetic factors are close to the nuclear contribution of 12.2 MHz/T because of lower second-order effects, as already observed above for the zero-field splittings.

D. Spin inhomogeneous and homogeneous linewidths

The evolution of the spin-echo amplitude as a function of the two-color frequency detuning is displayed in Fig. 5. Maximum spin-echo amplitudes were found for frequency detunings of 5.99 and 10.42 MHz, providing one order of magnitude better accuracy for the ground-state hyperfine splittings than hole burning experiments (Sec. III B). The analysis

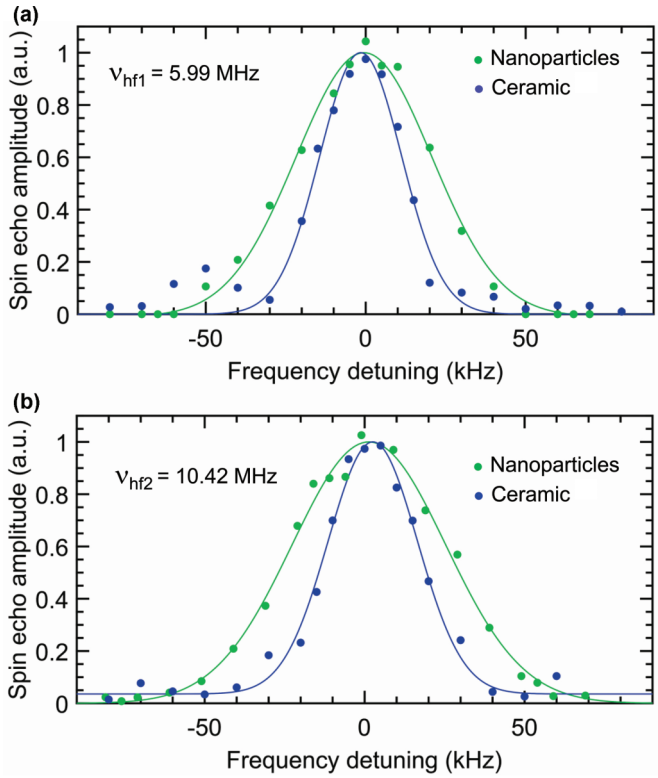

FIG. 5. Spin inhomogeneous linewidth obtained by two-pulse Raman spin echo at 1.4 K for ceramic (blue) and 400-/120-nm-diameter particles/crystallites (green). (a) $\pm 1/2 \leftrightarrow \pm 3/2$ transition at 5.99 MHz. (b) $\pm 3/2 \leftrightarrow \pm 5/2$ transition at 10.42 MHz. Lines correspond to curves fitted to the experimental data (dots).

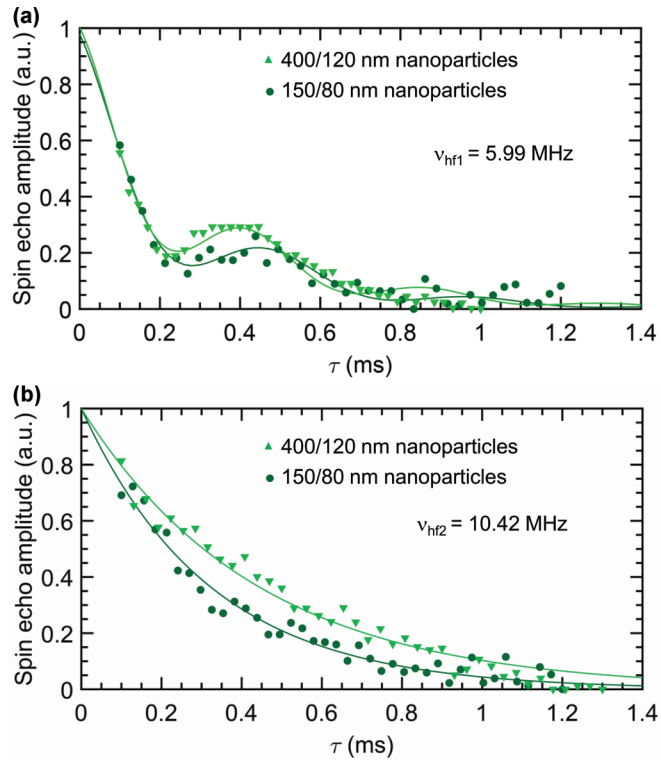

FIG. 6. Spin-echo decay curves at $T = 1.4$ K. (a) Spin-echo decay for the 5.99-MHz transition from 400-/120-nm-diameter particles/crystallites (light green triangles) and 150-/80-nm diameter particles/crystallites (dark green dots). Lines correspond to fits to Eq. (9). (b) Spin-echo decay for the 10.42-MHz transition for 400-nm (light green triangles) and 150-nm nanoparticles (dark green dots). Lines correspond to single-exponential fits.

gives a linewidth of 29 ± 2 kHz for both spin transitions in the ceramic sample, compatible with bulk Pr^{3+} : Y_2SiO_5 values [12]. In nanoparticles, larger spin inhomogeneous linewidths of 42 ± 9 and 48 ± 6 kHz were measured for the $\pm 1/2 \leftrightarrow \pm 3/2$ and the $\pm 3/2 \leftrightarrow \pm 5/2$ transitions, respectively. We believe that this can also be attributed to the O_2 plasma processing as nonprocessed Eu^{3+}-doped nanoparticles present spin inhomogeneous linewidths equivalent to ceramics [27] and bulk crystals [51].

Spin coherence lifetimes T_2 were finally obtained for both ground-state spin transitions at zero applied magnetic field. The decay of the spin-echo amplitude as a function of pulse delay τ is shown in Fig. 6 for both sizes of nanoparticles. Echo envelope modulation is clearly observed for the 5.99-MHz transition ($\pm 1/2 \leftrightarrow \pm 3/2$). This effect was previously reported in spin transitions of rare earths as due to the removal of the $\pm M_I$ degeneracy by residual magnetic fields [51]. Echo envelope modulation has also been attributed to superhyperfine coupling to surrounding nuclear spins [39,52]. The modulated spin-echo decays were fitted to the function [53]

$$E = Ae^{-2\tau/T_2}\,[1 + \mathrm{m}\cos^2(\omega\tau/2)], \qquad (9)$$

where m is the modulation amplitude and ω is the modulation frequency. Spin T_2 values of 680 ± 40 μs ($\Gamma_h = 470 \pm 50$ Hz) and 640 ± 40 μs ($\Gamma_h = 500 \pm 50$ Hz) were obtained from a fit to Eq. (9) in the 400-/120- and 150-/80-nm-diameter particles/crystallites, respectively. These values are longer than the reported zero-field spin coherence lifetimes in bulk Pr^{3+} : Y_2SiO_5 [54]. The modulation frequency $\omega/2\pi$ was found to be equal to 2.5 kHz. Unlike Fig. 6(a), no clear modulation is observed in the $\pm 3/2 \leftrightarrow \pm 5/2$ spin-echo decays at 10.42 MHz [Fig. 6(b)]. Thus, coherence lifetimes were straightforwardly derived by a single-exponential fit, yielding spin T_2 values of 880 ± 40 μs ($\Gamma_h = 360 \pm 40$ Hz) for the larger-diameter particles and 640 ± 30 μs ($\Gamma_h = 500 \pm 40$ Hz) for the 150-/80-nm-diameter ones. Spin-echo modulations can be expected as long as nuclear Zeeman splittings are comparable to the superhyperfine interaction [55]. Since splittings are larger for levels with larger M_J, this could explain why modulation is observed for only the $\pm 1/2 \leftrightarrow \pm 3/2$ transition.

E. Discussion

The relaxation and coherence properties demonstrated here for $^{141}Pr^{3+}$ in nanoscale Y_2O_3 appear very appealing for applications of this material in quantum devices. The results are summarized in Table III. Among them, the long spin dephasing times found in nanoparticles at zero external magnetic field are particularly promising. Unlike the optical transition, spin transitions are rather insensitive to electric perturbations given by their low nuclear Stark coefficient: three orders of magnitude lower than the optical one [56,57]. Thus, spin dephasing is here most likely due to magnetic interactions,

TABLE III. Summary of spectral and relaxation parameters determined for the $^{141}Pr^{3+}:Y_2O_3$ ceramic and two sizes of nanoparticles. Spin T_2 values for the ceramic sample, not displayed in Fig. 6, are given for the sake of comparison.

	Ceramic	400/120 nm	150/80 nm
Optical			
Γ_{inh} (GHz)	9	27	
T_1 (μs)	140	140	
T_2 (μs)	4.5 ± 0.5	3.0 ± 0.3	1.0 ± 0.1
$\Gamma_{h,opt}$ (kHz)	72 ± 16	108 ± 21	315 ± 64
Spin			
T_1 (s)	5 ± 1	7 ± 3	
$\Gamma_{inh,5.99}$ (kHz)	29 ± 2	42 ± 9	
$\Gamma_{inh,10.42}$ (kHz)	29 ± 2	48 ± 6	
$T_{2,5.99}$ (μs)	730 ± 50	680 ± 40	640 ± 40
$\Gamma_{h,5.99}$ (Hz)	440 ± 60	470 ± 50	500 ± 50
$T_{2,10.42}$ (μs)	730 ± 20	880 ± 40	640 ± 30
$\Gamma_{h,10.42}$ (Hz)	430 ± 30	360 ± 40	500 ± 40

as concluded for $Eu^{3+}:Y_2O_3$ nanoparticles [27] and, in general, for many bulk rare-earth-doped crystals [51]. Still, in view of the present results, the magnetic sensitivity of Pr^{3+} in Y_2O_3 appears to be lower than in other crystalline hosts, including Y_2SiO_5. This can be explained by the larger crystal-field splitting in Y_2O_3 compared to other materials. As mentioned in Sec. III C, this gives rise to lower second-order contributions and results in smaller hyperfine splittings and gyromagnetic ratios (Tables I and II). Furthermore, we note that the spin coherence results presented here are obtained not from bulk single crystals, but from nanoparticles down to 150 nm. Hence, $Pr^{3+}:Y_2O_3$ is a high-performing material at the nanoscale. As a main drawback, the small hyperfine splittings of Pr^{3+} in Y_2O_3, especially in the excited state (Fig. 4), limit the minimum optical pulse length which can be used in quantum memory schemes to about 500 ns. Taking into account the measured optical coherence lifetimes, in the few-microsecond range (Fig. 2), shorter pulses would be ideally required to limit dephasing in the excited state in spin-wave quantum memory schemes [12]. As a solution, optical T_2 enhancement can be envisioned. So far, optical coherence lifetimes in nanoparticles does not appear to be fundamentally limited [26], and we have already demonstrated that optical T_2 extension is obtained by postsynthesis treatments. Further improvement should therefore be possible by increasing the particle crystalline quality and reducing defects [58].

Apart from quantum storage applications, $Pr^{3+}:Y_2O_3$ nanoparticles coupled to optical microcavities appear to be promising candidates for realizing spin-photon interfaces emitting indistinguishable single photons. For this, a key parameter to determine is the effective Purcell factor $C = \xi \frac{3\lambda^3}{4\pi^2}\frac{Q}{V}$, where ξ is the branching ratio for the $^1D_2(0) \rightarrow {}^3H_4(0)$ transition [Fig. 7(a)], assumed here to be the only transition coupled to the cavity, Q is the cavity quality factor, V is the mode volume, and λ is the emission wavelength. ξ was derived from the T_1/T_{spon} ratio, with T_{spon} being the time it takes for the excited state to decay to the ground state through the enhanced transition [59]. To calculate T_{spon} we first determined the transition oscillator strength P for a single ion, which we found to be equal to 6.3×10^{-7}. We note that in a cubic crystal like Y_2O_3, P for a single ion is equivalent to three times the average oscillator strength obtained from the absorption spectrum. For $P = 6.3 \times 10^{-7}$, T_{spon} equals 2.5 ms, calculated using the expressions in [59]. Thus, with $T_1 = 140$ μs [Fig. 7(b)], we conclude that $\xi = 0.057$. For a realistic cavity presenting a finesse $\mathcal{F} = 10^5$ and the smallest mirror separation $d = 2$ μm, like the one discussed in [19], an effective Purcell factor $C = 340$ would be expected. This is more than three times higher than that expected for Eu^{3+}[19], mainly because of the difference in branching ratios between the Eu^{3+} and Pr^{3+} transitions. With such a Purcell factor, the demonstrated optical T_2 values in the 400- and 150-nm-diameter particles (Table III) already verify the condition to emit Fourier-transform-limited photons: $C > 2T_1/T_2$. However, in practice, achieving an effective Purcell factor $C = 340$ implies limiting cavity losses such as those due to scattering by the particles. In this sense, the particle size plays an important role; the smaller the particle size is, the lower the scattering losses are. In view of the present results (Table III), efforts should be made to reduce the particle size without decreasing the optical T_2.

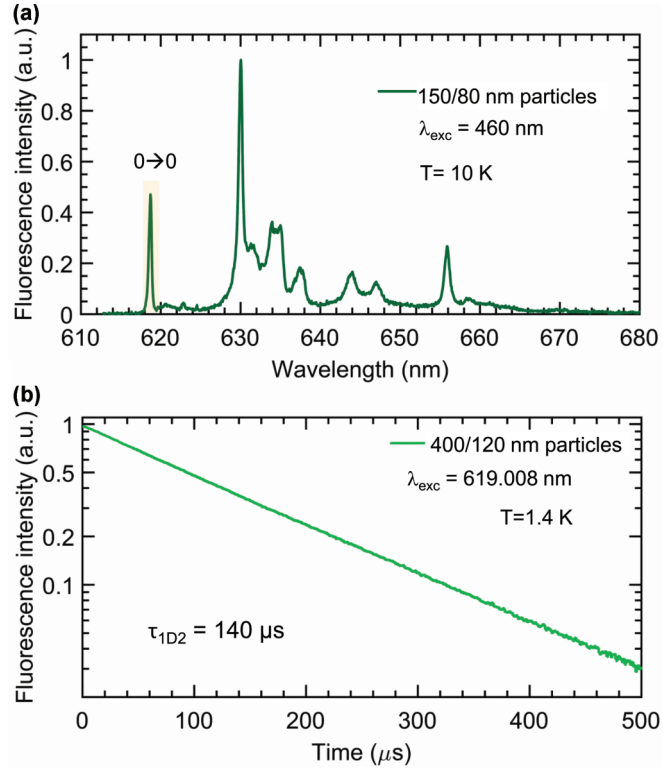

FIG. 7. Low-temperature fluorescence spectroscopy of $Pr^{3+}:Y_2O_3$ nanoparticles. (a) $^1D_2$ emissions in the 610–680-nm range. The peaks correspond to transitions towards different crystal field levels in the $^3H_4$ ground-state multiplet. The displayed spectrum is corrected from instrumental response. (b) $^1D_2$ fluorescence decay yielding an optical T_1 of 140 μs.

IV. CONCLUSION

In the present work we performed a complete high-resolution and coherent optical and spin spectroscopic

investigation of $^{141}Pr^{3+}:Y_2O_3$ ceramics and nanoparticles. We reported optical T_2 values of 3 and 1 μs for 400- and 150-nm-diameter particles, respectively. The hyperfine structure of $^{141}Pr^{3+}$ in Y_2O_3 was revealed by spectral hole burning and complete Hamiltonian numerical calculations. Ground-state spin transitions were assigned to 5.99 and 10.42 MHz, for which we demonstrated inhomogeneous linewidths of 42 and 48 kHz. Spin T_2 up to 880 μs was also obtained, a value which exceeds that of bulk Pr^{3+}-doped crystals such as Y_2SiO_5. We finally determined the oscillator strength and branching ratio for the $Pr^{3+}:{}^1D_2(0) \rightarrow {}^3H_4(0)$ in Y_2O_3. These results open up very interesting prospects for nanoscale $Pr^{3+}:Y_2O_3$, in particular as a candidate for quantum information storage and processing and source of indistinguishable single photons.

ACKNOWLEDGMENTS

This project received funding from the European Union Horizon 2020 research and innovation program under Grant Agreement No. 712721 (NanOQTech) and within the Flagship on Quantum Technologies with Grant Agreement No. 820391 (SQUARE). We thank G. Aka and R. Yasuhara for the transparent ceramic sample used in absorption measurements. Institut de Ciencies Fotoniques acknowledges financial support from the Gordon and Betty Moore Foundation through Grant No. GBMF7446 to H.d.R.

APPENDIX

The Hamiltonians used in the hyperfine-structure calculations (Sec. III C) are given below. The hyperfine interaction is expressed as

$$H_{HF} = a_1 H_1, \tag{A1}$$

where

$$a_1 = \frac{\mu_0}{4\pi} g_s \mu_B \mu_n g_n \langle r_e^{-3} \rangle. \tag{A2}$$

N and $\langle r_e^{-3} \rangle$ are the number and mean inverse cubic radius of the $4f$ electrons. Matrix elements of H_1, calculated using tensor operator techniques, are given in Ref. [48]. The quadrupolar interaction is divided into $4f$-electron (a_2H_2) and lattice field (a_3H_3) contributions:

$$H_Q = a_2 H_2 + a_3 H_3, \tag{A3}$$

with

$$a_2 = \frac{-e^2}{4\pi\epsilon_0}(1-R)\langle r_e^{-3} \rangle \frac{Q}{2}, \tag{A4}$$

$$a_3 = -\frac{(1-\gamma_\infty)}{(1-\sigma_2)\langle r_e^2 \rangle} \frac{Q}{2}. \tag{A5}$$

In these expressions, Q is the nuclear quadrupole moment; γ_∞, R, and σ_2 are shielding factors; and $\langle r_e^2 \rangle$ is the mean-square radius of the $4f$ electrons. More details and matrix elements for H_2 and H_3 can be found in Ref. [43].

[1] D. D. Awschalom, R. Hanson, J. Wrachtrup, and B. B. Zhou, Quantum technologies with optically interfaced solid-state spin, Nat. Photon. **12**, 516 (2018).

[2] D. D. Sukachev, A. Sipahigil, C. T. Nguyen, M. K. Bhaskar, R. E. Evans, F. Jelezko, and M. D. Lukin, Silicon-Vacancy Spin Qubit in Diamond: A Quantum Memory Exceeding 10 ms with Single-Shot State Readout, Phys. Rev. Lett. **119**, 223602 (2017).

[3] K. Saeedi, S. Simmons, J. Z. Salvail, P. Dluhy, H. Riemann, N. V. Abrosimov, P. Becker, H.-J. Pohl, J. J. L. Morton, and M. L. W. Thewalt, Room-temperature quantum bit storage exceeding 39 minutes using ionized donors in silicon-28, Science **342**, 830 (2013).

[4] C. Simon, M. Afzelius, J. Appel, A. Boyer de la Giroday, S. J. Dewhurst, N. Gisin, C. Y. Hu, F. Jelezko, S. Kröll, J. H. Müller, J. Nunn, E. S. Polzik, J. G. Rarity, H. De Riedmatten, W. Rosenfeld, A. J. Shields, N. Sköld, R. M. Stevenson, R. Thew, I. A. Walmsley, M. C. Weber, H. Weinfurter, J. Wrachtrup, and R. J. Young, Quantum memories, Eur. Phys. J. D **58**, 1 (2010).

[5] M. M. Zhong, M. P. Hedges, R. L. Ahlefeldt, J. G. Bartholomew, S. E. Beavan, S. M. Wittig, J. J. Longdell, and M. J. Sellars, Optically addressable nuclear spins in a solid with a six-hour coherence time, Nature (London) **517**, 177 (2015).

[6] G. Heinze, C. Hubrich, and T. Halfmann, Stopped Light and Image Storage by Electromagnetically Induced Transparency up to the Regime of One Minute, Phys. Rev. Lett. **111**, 033601 (2013).

[7] M. Rancic, M. P. Hedges, R. L. Ahlefeldt, and M. J. Sellars, Coherence time of over a second in a telecom-compatible quantum memory storage material, Nat. Phys. **14**, 50 (2018).

[8] C. W. Thiel, W. R. Babbitt, and R. L. Cone, Optical decoherence studies of yttrium oxyorthosilicate Y_2SiO_5 codoped with Er^{3+} and Eu^{3+} for optical signal processing and quantum information applications at 1.5 microns, Phys. Rev. B **85**, 174302 (2012).

[9] L. A. Williamson, Y.-H. Chen, and J. J. Longdell, Magneto-optic Modulator with Unit Quantum Efficiency, Phys. Rev. Lett. **113**, 203601 (2014).

[10] M. P. Hedges, J. J. Longdell, Y. Li, and Ma. J. Sellars, Efficient quantum memory for light, Nature (London) **465**, 1052 (2010).

[11] F. Bussieres, C. Clausen, A. Tiranov, B. Korzh, V. B. Verma, S. W. Nam, F. Marsili, A. Ferrier, P. Goldner, H. Herrmann, C. Silberhorn, W. Sohler, M. Afzelius, and N. Gisin, Quantum teleportation from a telecom-wavelength photon to a solid-state quantum memory, Nat. Photon. **8**, 775 (2014).

[12] M. Gundogan, P. M. Ledingham, K. Kutluer, M. Mazzera, and H. de Riedmatten, Solid State Spin-Wave Quantum Memory for Time-Bin Qubits, Phys. Rev. Lett. **114**, 230501 (2015).

[13] L. Rippe, B. Julsgaard, A. Walther, Y. Ying, and S. Kroll, Experimental quantum-state tomography of a solid-state qubit, Phys. Rev. A **77**, 022307 (2008).

[14] J. H. Wesenberg, K. Mølmer, L. Rippe, and S. Kroll, Scalable designs for quantum computing with rare-earth-ion-doped crystals, Phys. Rev. A **75**, 012304 (2007).

[15] T. Zhong, J. M. Kindem, J. G. Bartholomew, J. Rochman, I. Craiciu, V. Verma, S. W. Nam, F. Marsili, M. D. Shaw, A. D. Beyer, and A. Faraon, Optically Addressing Single Rare-Earth Ions in a Nanophotonic Cavity, Phys. Rev. Lett. **121**, 183603 (2018).

[16] A. M. Dibos, M. Raha, C. M. Phenicie, and J. D. Thompson, Atomic Source of Single Photons in the Telecom Band, Phys. Rev. Lett. **120**, 243601 (2018).

[17] R. Kolesov, K. Xia, R. Reuter, R. Stohr, A. Zappe, J. Meijer, P. R. Hemmer, and J. Wrachtrup, Optical detection of a single rare-earth ion in a crystal, Nat. Commun. **3**, 2034 (2012).

[18] E. Eichhammer, T. Utikal, S. Gotzinger, and V. Sandoghdar, Spectroscopic detection of single Pr^{3+} ions on the $^3H_4$-$^1D_2$ transition, New J. Phys. **17**, 083018 (2015).

[19] B. Casabone, J. Benedikter, T. Hümmer, F. Oehl, K. de Oliveira Lima, T. W. Hänsch, A. Ferrier, P. Goldner, H. de Riedmatten, and D. Hunger, Cavity-enhanced spectroscopy of a few-ion ensemble in Eu^{3+} : Y_2O_3, New J. Phys. **20**, 095006 (2018).

[20] M. J. Burek, C. Meuwly, R. E. Evans, M. K. Bhaskar, A. Sipahigil, S. Meesala, B. Machielse, D. D. Sukachev, C. T. Nguyen, J. L. Pacheco, E. Bielejec, M. D. Lukin, and M. Loncar, Fiber-Coupled Diamond Quantum Nanophotonic Interface, Phys. Rev. Appl. **8**, 024026 (2017).

[21] H. S. Knowles, D. M. Kara, and M. Atatüre, Observing bulk diamond spin coherence in high-purity nanodiamonds, Nat. Mater. **13**, 21 (2014).

[22] T. Lutz, L. Veissier, C. W. Thiel, P. J. T. Woodburn, R. L. Cone, P. E. Barclay, and W. Tittel, Effects of mechanical processing and annealing on optical coherence properties of Er^{3+} : $LiNbO_3$ powders, J. Lumin. **191**, 2 (2017).

[23] R. S. Meltzer, H. Zheng, and M. J. Dejneka, Photon echo studies of LaF_3 : Pr^{3+} nanocrystals in glass, J. Lumin. **107**, 166 (2004).

[24] K. de Oliveira Lima, R. Rocha Goncalves, D. Giaume, A. Ferrier, and P. Goldner, Influence of defects on sub-GHz optical linewidths in Eu^{3+} : Y_2O_3 particles, J. Lumin. **168**, 276 (2015).

[25] S. Liu, D. Serrano, A. Fossati, A. Tallaire, A. Ferrier, and P. Goldner, Controlled size reduction of rare earth doped nanoparticles for optical quantum technologies, RSC Adv. **8**, 37098 (2018).

[26] J. G. Bartholomew, K. de Oliveira Lima, A. Ferrier, and P. Goldner, Optical line width broadening mechanisms at the 10 kHz level in Eu^{3+} : Y_2O_3 nanoparticles, Nano Lett. **17**, 778 (2017).

[27] D. Serrano, J. Karlsson, A. Fossati, A. Ferrier, and P. Goldner, All-optical control of long-lived nuclear spins in rare-earth doped nanoparticles, Nat. Commun. **9**, 2127 (2018).

[28] C. A. Morrison, R. P. Leavitt, J. B. Gruber, and N. C. Chang, Optical spectra, energy levels, and crystal-field analysis of tripositive rare-earth ions in Y_2O_3. III. Intensities and g values for C2 sites, J. Chem. Phys. **79**, 4758 (1983).

[29] W. F. Krupke, Optical absorption and fluorescence intensities in several rare-earth-doped Y_2O_3 and LaF_3 single crystals, Phys. Rev. **145**, 325 (1966).

[30] Y. Guyot, R. Moncorge, L. D. Merkle, A. Pinto, B. McIntosh, and H. Verdun, Luminescence properties of Y_2O_3 single crystals doped with Pr^{3+} or Tm^{3+} and codoped with Yb^{3+}, Tb^{3+} or Ho^{3+} ions, Opt. Mater. **5**, 127 (1996).

[31] T. Okuno, K. Tanaka, K. Koyama, M. Namiki, and T. Suemoto, Homogeneous line width of Praseodymium ions in various inorganic materials, J. Lumin. **58**, 184 (1994).

[32] T. Okuno and T. Suemoto, Two types of spectral holes in Y_2O_3 : Pr^{3+} crystalline systems, J. Lumin. **66-67**, 179 (1995).

[33] T. Okuno and T. Suemoto, Systematic control of spectral hole burning and homogeneous linewidth by disorder in Y_2O_3 : Pr^{3+} crystalline systems, Phys. Rev. B **59**, 9078 (1999).

[34] S. Liu, A. Fossati, D. Serrano, A. Tallaire, A. Ferrier, and P. Goldner, Defect engineering for quantum grade rare-earth nanocrystals (unpublished).

[35] A. Perrot, Ph. Goldner, D. Giaume, M. Lovric, C. Andriamiadamanana, R. R. Concalves, and A. Ferrier, Narrow Optical Homogeneous Linewidths in Rare Earth Doped Nanocrystals, Phys. Rev. Lett. **111**, 203601 (2013).

[36] R. W. Equall, R. L. Cone, and R. M. Macfarlane, Homogeneous broadening and hyperfine structure of optical transitions in Pr^{3+} : Y_2SiO_5, Phys. Rev. B **52**, 3963 (1995).

[37] P. Goldner, A. Ferrier, and O. Guillot-Noel, Rare earth-doped crystals for quantum information processing, Handb. Phys. Chem. Rare Earths **46**, 1 (2015).

[38] R. Klieber, A. Michalowski, R. Neuhaus, and D. Suter, All-optical measurement of nuclear-spin relaxation, Phys. Rev. B **68**, 054426 (2003).

[39] M. Lovrić, P. Glasenapp, D. Suter, B. Tumino, A. Ferrier, P. Goldner, M. Sabooni, L. Rippe, and S. Kröll, Hyperfine characterization and spin coherence lifetime extension in Pr^{3+} : $La_2(WO_4)_3$, Phys. Rev. B **84**, 104417 (2011).

[40] K. Holliday, M. Croci, E. Vauthey, and U. P. Wild, Spectral hole burning and holography in an Y_2SiO_5 : Pr^{3+} crystal, Phys. Rev. B **47**, 14741 (1993).

[41] L. Petersen, High resolution spectroscopy of Pr^{3+} ions in a solid state matrix, Ph.D. thesis, ETH Zurich, 2011.

[42] M. Gündogan, Solid-state quantum memory for photonic qubits, Ph.D. thesis, Institut de Ciencies Fotoniques, 2015, Chap. 2.

[43] O. Guillot-Noël, Y. Le Du, F. Beaudoux, E. Antic-Fidancev, M. F. Reid, R. Marino, J. Lejay, A. Ferrier, and Ph. Goldner, Calculation and analysis of hyperfine and quadrupole interactions in praseodymium-doped $La_2(WO_4)_3$, J. Lumin. **130**, 1557 (2010).

[44] R. Marino, I. Lorgere, O. Guillot-Noël, H. Vezin, A. Toncelli, M. Tonelli, J.-L. Le Gouët, and P. Goldner, Energy level structure and optical dephasing under magnetic field in Er^{3+} : $LiYF_4$ at 1.5μm, J. Lumin. **169**, 478 (2016).

[45] S. P. Horvath, J. V. Rakonjac, Y.-H. Chen, J. J. Longdell, P. Goldner, J.-P. R. Wells, and M. F. Reid, Extending Phenomenological Crystal-Field Methods to C_1 Point-Group Symmetry: Characterization of the Optically Excited Hyperfine Structure of $^{167}Er^{3+}$: Y_2SiO_5, Phys. Rev. Lett. **123**, 057401 (2019).

[46] J.-P. R. Wells, G. D. Jones, M. F. Reid, M. N. Popova, and E. P. Chukalina, Hyperfine patterns of infrared absorption lines of Ho^{3+} C_{4v} centres in CaF_2, Mol. Phys. **102**, 1367 (2004).

[47] P. Goldner and O. Guillot-Noël, Magnetic interactions in Pr^{3+} : $LiYF_4$ for quantum manipulation: Search for an efficient λ system, Mol. Phys. **102**, 1185 (2004).

[48] O. Guillot-Noël, P. Goldner, E. Antic-Fidancev, and J. L. Le Gouet, Analysis of magnetic interactions in rare-earth-doped crystals for quantum manipulation, Phys. Rev. B **71**, 174409 (2005).

[49] J. J. Longdell, M. J. Sellars, and N. B. Manson, Hyperfine interaction in ground and excited states of praseodymium-doped yttrium orthosilicate, Phys. Rev. B **66**, 035101 (2002).

[50] M. Lovrić, P. Glasenapp, and D. Suter, Spin Hamiltonian characterization and refinement for Pr^{3+} : $YAlO_3$ and Pr^{3+} : Y_2SiO_5, Phys. Rev. B **85**, 014429 (2012).

[51] A. Arcangeli, M. Lovrić, B. Tumino, A. Ferrier, and P. Goldner, Spectroscopy and coherence lifetime extension of hyperfine transitions in $^{151}Eu^{3+}$: Y_2SiO_5, Phys. Rev. B **89**, 184305 (2014).

[52] E. Fraval, M. J. Sellars, A. Morrison, and A. Ferris, Pr-Y interaction in Pr^{3+} : Y_2SiO_5, J. Lumin. **107**, 347 (2004).

[53] K. Karlsson, N. Kunkel, A. Ikessue, A. Ferrier, and P. Goldner, Nuclear spin coherence properties of $^{151}Eu^{3+}$ and $^{153}Eu^{3+}$ in a Y_2O_3 transparent ceramic, J. Phys.: Condens. Matter **29**, 125501 (2017).

[54] E. Fraval, M. J. Sellars, and J. J. Longdell, Method of Extending Hyperfine Coherence Times in Pr^{3+} : Y_2SiO_5, Phys. Rev. Lett. **92**, 077601 (2004).

[55] B. Car, L. Veissier, A. Louchet-Chauvet, J.-L. Le Gouët, and T. Chanelière, Selective Optical Addressing of Nuclear Spins Through Superhyperfine Interaction in Rare-Earth Doped Solids, Phys. Rev. Lett. **120**, 197401 (2018).

[56] R. M. Macfarlane, A. Arcangeli, A. Ferrier, and P. Goldner, Optical Measurement of the Effect of Electric Fields on the Nuclear Spin Coherence of Rare-Earth Ions in Solids, Phys. Rev. Lett. **113**, 157603 (2014).

[57] F. R. Graf, A. Renn, U. P. Wild, and M. Mitsunaga, Site interference in stark-modulated photon echoes, Phys. Rev. B **55**, 11225 (1997).

[58] N. Kunkel, A. Ferrier, C. W. Thiel, M. O. Ramirez, L. E. Bausa, R. L. Cone, A. Ikesue, and P. Goldner, Rare-earth doped transparent ceramics for spectral filtering and quantum information processing, APL Mater. **3**, 096103 (2015).

[59] D. L. McAuslan, J. J. Longdell, and M. J. Sellars, Strong-coupling cavity QED using rare-earth-metal-ion dopants in monolithic resonators: What you can do with a weak oscillator, Phys. Rev. A **80**, 062307 (2009).